Numerical simulation of lifted tribrachial *n*-heptane laminar flames in heated coflow

M. Toma, F. Bisetti*, S.M. Sarathy, S.K. Choi, S. Al-Noman and S.H. Chung

Clean Combustion Research Center, King Abdullah University of Science and Technology, Saudi Arabia

Abstract

This study presents a numerical analysis of lifted atmospheric tribrachial flames in heated coflow in a two-dimensional axisymmetric domain. A reduced mechanism for *n*-heptane/air combustion comprising 97 species is used together with a mixture-averaged transport model. The chemical mechanism is complemented with the chemiluminescent OH (OH*) and CH (CH*) reaction pathways. The mechanism is validated. A parametric study of lift-off height of the tribrachial flame is performed for a range of temperatures, jet velocities and fuel compositions. The lift-off height dependence on inlet temperature is compared with preliminary experimental data showing excellent agreement. A preliminary comparison of the line-of-sight integrated CH* fields from the simulations with narrow-band filtered photographs is presented.

Introduction

Tribrachial flames are characteristic of fuel/air mixing layers with concentration gradients [1]. Such flames exhibit a well-defined structure, comprising two distinct premixed flame wings, one lean and one rich, together with a trailing diffusion flame, all stemming from a single point (tribrachial point), see Fig. 1. Tribrachial flames have been observed in a variety of combustion problems, including direct numerical simulations of turbulent combustion, heterogeneous propellant combustion, and jet flames. Tribrachial flame propagation has been proposed as a key mechanism contributing to the stabilisation and dynamics of various laminar and turbulent flame configurations.

Tribrachial flames develop in laminar jet flames, whereby a fuel jet issues in a coflowing oxidiser stream and a stratified mixing layer is formed at the interface. The development, stabilisation, and propagation of tribrachial flames in laminar jets of various gaseous and liquid fuels has been studied extensively in well-defined experiments [1–4].

Numerical calculations [1, 5] of tribrachial flames typically involve significant simplifications to the kinetic mechanism describing fuel oxidation. A number of simulations of tribrachial flames with one- and multi-step chemistry are available in the literature. Additional simplifications include the use of constant Lewis number assumptions in the treatment of the diffusive fluxes. The recent work of [5] is an exception. The authors simulated a set of two *n*-heptane/air flames in a stratified mixture with finite rate chemistry and detailed transport and analysed the reaction pathways at several locations in the flame with the aim of elucidating the most important chemical reactions in the premixed and diffusion flame segments.

The goal of this study is two-fold. Firstly, we wish to simulate a tribrachial flame of *n*-heptane in a laboratory configuration for which experimental data generated in our laboratory is available [6]. The simulation features a reduced *n*-heptane/air kinetic mechanism for the high-temperature regime and mixture-average transport. The configuration consists of a diluted *n*-heptane/nitrogen jet issuing in coflowing air. Both the fuel and oxidiser streams are at atmospheric pressure and preheated to a temperature ranging from 500 to 700 K. As the inlet temperature, jet velocity, and dilution ratio are varied, the stabilisation height of the tribrachial flame (lift-off height) is recorded. In this work, the lift-off height of the stabilised flame is recovered as part of the simulation and compared with experiments for various conditions.

Secondly, the *n*-heptane high-temperature oxidation chemistry is complemented by a recently published mechanism for CH^* and OH^* [7]. The chemiluminescence originating from the excited species is simulated and compared with experimental images of the flame. The synthetic chemiluminescence signal from the simulation is correlated with the spatial distribution of the heat release rate and shown to provide an excellent indication of the structure of the reaction zone and flame sheet.

Chemical kinetic model formulation

The skeletal *n*-heptane/air combustion mechanism used comprises 97 species and has been developed for applicability in the temperature and pressure range of the tribrachial flame experiments. The mechanism is based on the detailed large alkanes combustion model from the Lawrence Livermore National Laboratory [8], with added detailed chemiluminescent OH and CH reaction pathways [7]. The mechanism is reduced using the DRG approach [9]. The reduction is performed based on reaction states sampled in a parameter range that is relevant to the flames studied in the present work. The reaction states are sampled from auto-ignition calculated with SENKIN and from perfectly stirred reactors (PSR). Both applications are simulated under atmospheric pressure *n*-heptane/air mixtures with equivalence ratios between 0.5 and 2.0. The initial temperature for ignition is set to be

Corresponding author: fabrizio.bisetti@kaust.edu.sa
Proceedings of the European Combustion Meeting 2013

1000-1800 K. The inlet temperature for PSR is fixed at 300 K, which yields reactor temperatures of 1000-2300 K for 1 atm and the stoichiometry considered. These temperature ranges are chosen to cover the temperature ranges expected in the lifted tribrachial flames. This leads to a reduced mechanism consisting of approximately 150 species. The mechanism, generated by the DRG reduction, is further reduced by manually tracking the consumption of fuel radicals, alkenes, and alkenyl radicals towards the formation of smaller hydrocarbon species. Any small molecules (C1-C4) that are not directly linked with the reactivity of *n*-heptane are manually removed from the mechanism. A special focus is placed on retaining the chemical fidelity of small molecules that are important to the production and consumption of excited state molecules (CH* and OH*).

2-D simulation methods

The gas phase hydrodynamics are modelled with the reactive, unsteady Navier-Stokes equations in the low Mach number limit [10], solved on a structured axisymmetric grid. In the present work, the transport of species mass fractions is described using the Hirschfelder and Curtiss approximation to the diffusive fluxes [11, 12] together with a velocity-correction approach [13] to enforce mass conservation. Soret and Dufour effects are neglected. The species mass fraction and temperature equations read

$$\frac{\partial \rho Y_i}{\partial t} + \nabla \cdot (\rho \mathbf{u} Y_i) = -\nabla \cdot (\rho Y_i \mathbf{V}_i) + \dot{\omega}_i \qquad (1)$$

and

$$c_p \left[\frac{\partial \rho T}{\partial t} + \nabla \cdot (\rho \mathbf{u} T) \right] = \nabla \cdot (\lambda \nabla T) - \sum_{i=1}^{M} c_{p,i} (\rho Y_i \mathbf{V}_i) \cdot \nabla T + \dot{\omega}_T. \qquad (2)$$

In Eq. (1) and Eq. (2), the mass-based species velocity $\mathbf{V}_i$ is defined as

$$\mathbf{V}_i = -D_i^m \frac{\nabla X_i}{X_i}, \qquad (3)$$

where X_i and D_i^m are the mole fraction and mixture-average diffusion coefficient of species i, respectively. The thermal conductivity is λ, c_p is the mixture specific heat at constant pressure, and $c_{p,i}$ are the specific heats for each species. The terms $\dot{\omega}_i$ and $\dot{\omega}_T$ indicate source terms for species mass fractions and temperature, respectively.

The parallel flow solver "NGA" [14], developed at Stanford University, is used to solve the transport equations. The solver implements a finite difference method on a spatially and temporally staggered grid with the semi-implicit fractional-step method [15]. Velocity and scalar spatial derivatives are discretised with a second order finite differences centred scheme. The time step size is calculated to achieve the unity CFL number. The solution of the Poisson equation on massively parallel machines is performed by the library *hypre* [16] with the preconditioned conjugate gradient iterative solver [17] coupled with one iteration of a multi-grid pre-conditioner [18].

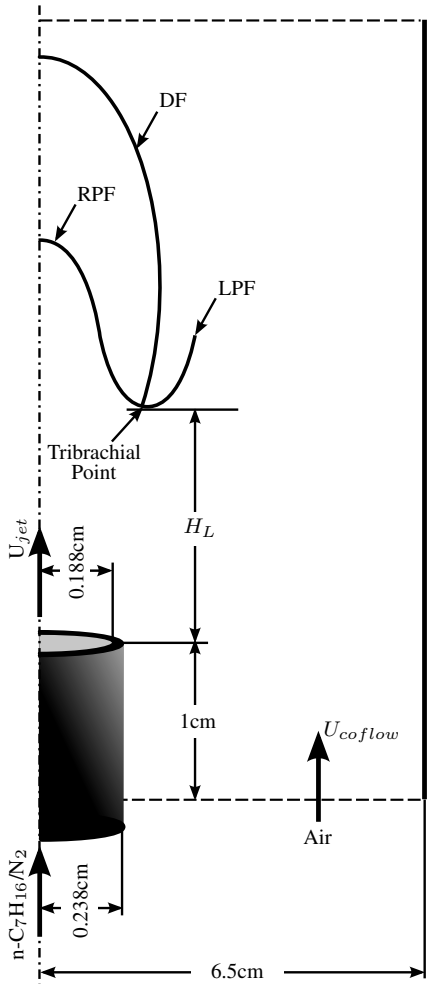

Figure 1: Experimental and computational configuration and the tribrachial flame structure, the rich premixed flame (RPF), lean premixed flame (LPF) and diffusion flame (DF) are labeled.

Experimental and numerical configuration

The computational configuration reflects the experimental setup. The targeted fuel is diluted *n*-heptane/nitrogen in a co-flow of air. The reactive Navier-Stokes equations in the low Mach number limit are solved in a two-dimensional axisymmetric domain with 6.5 cm width from the axis of symmetry, the burner inner and outer radii of 0.188 and 0.238 cm, respectively, and the length of the burner 1 cm, see Fig. 1. Two mesh configurations are used. Basic, less refined, mesh (422x210 grid points, locally refined around the maximum gradients) is used to run the calculations to meet the steady solution. Consequently, if necessary, restart function is used to run the calculations further with a mesh of the grid points doubled in both directions. The time required for the simulations is between 6000 to 12000 CPU hours in order to reach the steady solution on the basic, less refined, mesh. Additional around 3000 CPU hours are used

to run the computations on more refined mesh, if necessary to smoothen the solution. All simulations are performed with 128 processors on a Linux Cluster equipped with Infiniband interconnect and Intel Xeon X5570 quad-core processors with 2.93 GHz clock rate.

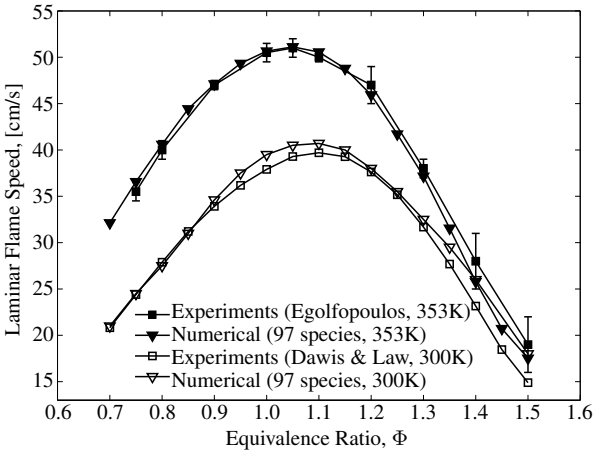

Figure 2: Comparison of experimental [19, 20], respectively, and computed laminar flame speed of *n*-heptane/air mixture at ambient pressure.

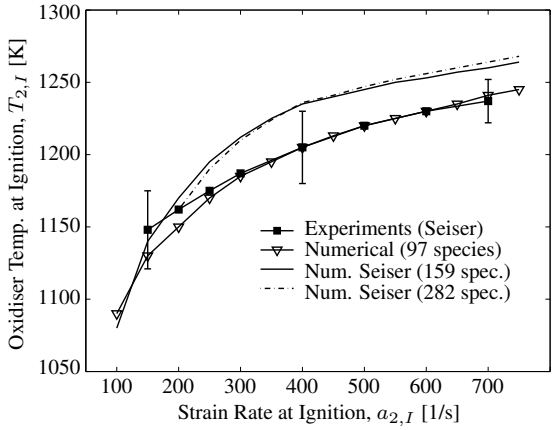

Figure 3: Comparison of experimental [21] and computed oxidiser temperature at autoignition, $T_{2,I}$, as a function of the strain rate, $a_{2,I}$.

Chemical kinetic model validation

The chemical and transport models are validated against published experimental data [19–21], using CHEMKIN [22, 23], as shown in Figs. 2 and 3. Fig. 2 shows the comparison of the present mechanism and the experimental data obtained with non-linear extrapolation [24] at atmospheric pressure and temperatures of 353 K [19] and 300 K [20]. Excellent agreement with the experimental results, specially near the stoichiometric mixtures where the experimental uncertainties are smaller, can be observed.

Moreover, the experimental results and calculations from the study on the mechanism of autoignition of *n*-heptane in opposed flow configuration [21] are compared with the present 97-species model, using CHEMKIN, in Fig. 3. The momenta of the opposed flow reactant streams at the duct exits are kept equal to hold the flame approximately in the middle of the two ducts [25]. Again, excellent agreement with the experimental results is found, wherein the present model predictions fall within the uncertainty of the experimental measurements.

T_0 $[K]$	U_{jet} $[m/s]$	$U_{cofl.}$ $[m/s]$	$X_{nhep,f}$ -	$H_L^{exp.}$ $[mm]$	$H_L^{num.}$ $[mm]$
500	1.5	0.4	0.035	108.4	107.5
525	1.5	0.4	0.035	-	89.5
550	1.5	0.4	0.035	-	74.0
575	1.5	0.4	0.035	-	60.6
600	1.4	0.4	0.035	41.5	50.4
600	1.5	0.4	0.030	54.6	57.2
600	1.5	0.4	0.035	48.2	53.8
600	1.5	0.4	0.040	41.6	50.0
600	1.6	0.4	0.035	54.0	58.2
625	1.5	0.4	0.035	-	47.3
650	1.5	0.4	0.035	-	38.0
675	1.5	0.4	0.035	-	30.5
700	1.5	0.4	0.035	24.0	24.0

Table 1: Parameters used for the experiments and simulations, and the resulting experimental and numerical flame heights.

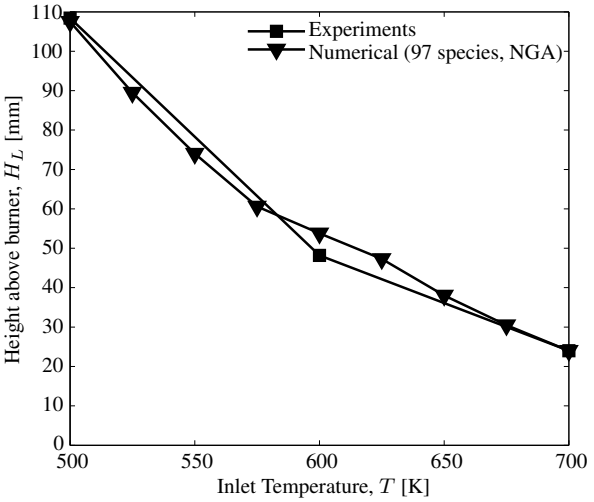

Figure 4: Experimental and numerical height above the burner, H, as a function of the inlet temperature, T, with $U_{jet} = 1.5\ m/s$, $U_{coflow} = 0.4\ m/s$, $X_{n-hep,f} = 0.035$.

Lift-off height dependence

To compare the flame behaviour to a high-quality database of experiments and to study the lift-off height dependence, the numerical model predictions are evaluated for various configurations, using the parallel flow solver "NGA". In each configuration, either the inlet jet bulk velocity, U_{jet}, the inlet temperature, T_0, or the fuel mole fraction, $X_{n-hep,f}$, is varied. Table 1 reports the various cases. The resulting Reynolds numbers are below 100. The lift-off height, H_L, is measured as the distance between the burner and the edge of the flame, as depicted in Fig. 1.

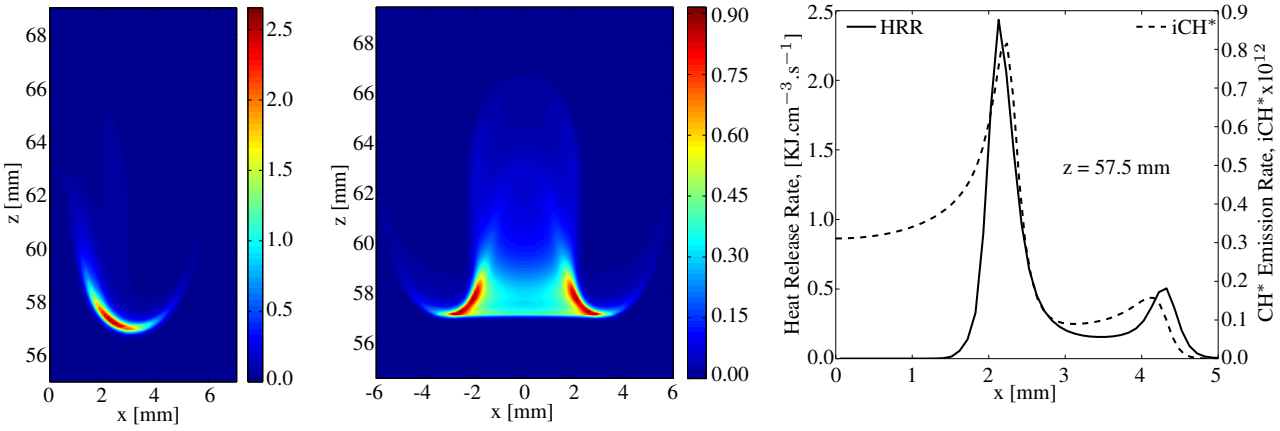

(a) Heat Release Rate (b) iCH* (c) Horizontal cut

Figure 5: The correlation between the heat release rate and the line-of-sight integrated CH*, with $T_0 = 625\ K$, $U_{jet} = 1.5\ m/s$, $U_{coflow} = 0.4\ m/s$, $X_{n-hep,f} = 0.035$.

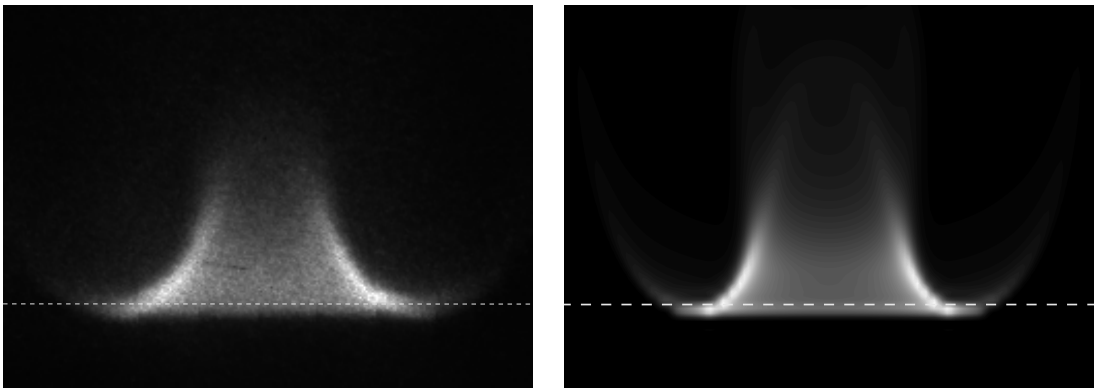

(a) Experiment (b) Simulation

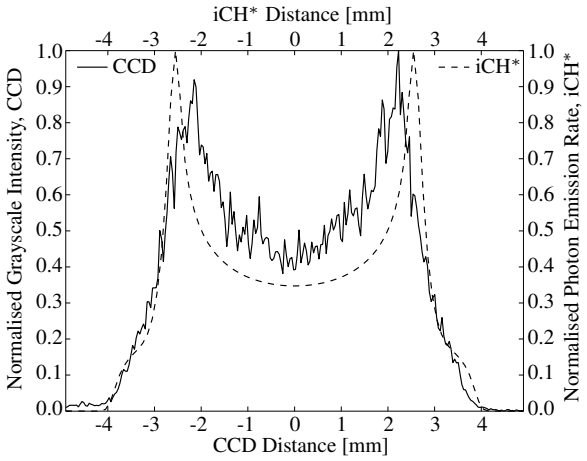

(c) Horizontal cut

Figure 6: Narrow-band (431 nm) filtered photograph of CH* (a) and numerical results, the mass fraction of CH* species after line-of-sight integration, (b), and the grayscale intensity values along the dashed lines in the CCD photograph compared with the numerical results of mass fraction of CH* (c), with $T_0 = 600\ K$, $U_{jet} = 1.5\ m/s$, $U_{coflow} = 0.4\ m/s$, $X_{n-hep,f} = 0.035$.

According to results summarised in Table 1, depending on the inlet temperature the flame lift-off height is between $24 < H_L < 108$ mm, thus decreasing with the increasing temperature. Similarly, with the inlet jet velocity or fuel composition increasing, the lift-off height increases or decreases, respectively. The comparison of the experimental and numerical results, using "NGA", is shown in Fig. 4. The comparison of lift-off height indicates less than 5 % difference with the experiments. At this point, it is convenient to recall that these are 2D simulations with complex chemical mechanism of high hydrocarbon fuel and complex numerics resulting in a flame of complex tribrachial structure.

Chemiluminescence

Chemiluminescence is light emitted by molecules chemically created in an excited energy state. It is an optical (non-intrusive) diagnostic tool and it can be used, e.g, as a heat release rate marker [26]. Common chemiluminescent species in hydrocarbon/air flames are CH*, OH*, C_2^* and CO_2^*. In the present mechanism, the CH* and OH* species are included as it is sufficient for the purpose of this study. As mentioned, it is known there is a correlation between the chemiluminescent species CH* and heat release rate. From the practical perspective, considering that measuring heat release rate is nearly impossible, it is easier to just take a photograph of the flame. Therefore, having the means of marking the heat release rate using the optical tools, e.g. taking photographs of the CH* species, can be rather beneficial.

However, to compare the numerical results with the photographs, the spatially-resolved information has to be convoluted to the line-of-sight projection data [27, 28], see Fig. 5 showing the comparison of heat release rate and line-of-sight integrated CH*. In this study, the numerical results, namely the mass fraction of the CH* species, are post-processed (line-of-sight integrated and mirrored around the axis of symmetry to complete the full flame image) to be compared with the photographs of the flame taken through a narrow-band filter isolating the given frequencies. The CH* and OH* emit near 431 nm and 308 nm, respectively. The horizontal cuts, across the heat release rate and the line-of-sight integrated CH*, Figs. 5(a) and 5(b) respectively, show that the relative proportions between the rich and lean premixed wings are well correlated, as shown in Fig. 5(c).

Fig. 6(a) shows the CCD imagine of the tribrachial flame with initial temperature of 600 K, taken through narrow-band filter isolating the frequencies to near 431 nm. Using the same configuration, the "NGA" is used to obtain the equivalent results numerically. The output of the line-of-sight integration, post-processed numerical results, is shown in the Fig. 6(b).

The grayscale intensity values of the photograph are extracted along the dashed line depicted in Fig. 6(a) and compared with the computed values along the dashed line in similar position in Fig. 6(b). The Fig. 6(c) shows the comparison. The CCD distance, in Fig. 6(c), is converted from pixels to mm by taking the photograph of a ruler under the same configuration.

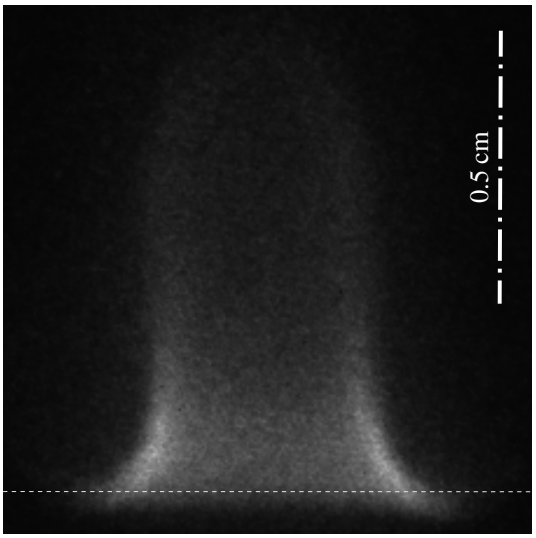

Figure 7: Narrow-band (431 nm) filtered photograph of CH*, with $T_0 = 700\ K$, $U_{jet} = 1.5\ m/s$, $U_{coflow} = 0.4\ m/s$, $X_{n-hep,f} = 0.035$.

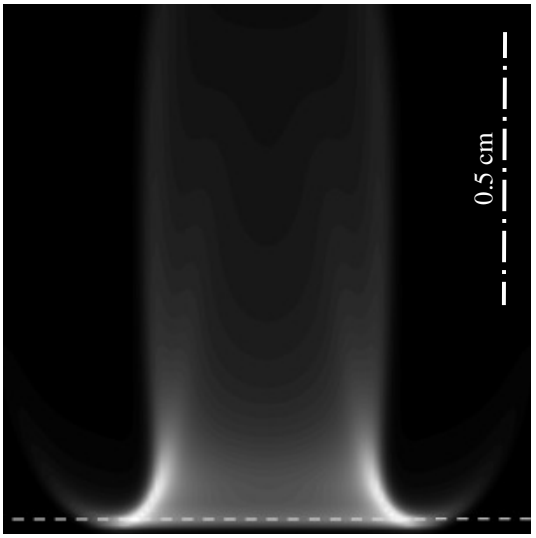

Figure 8: Numerical results, the mass fraction of CH* species after line-of-sight integration, with $T_0 = 700\ K$, $U_{jet} = 1.5\ m/s$, $U_{coflow} = 0.4\ m/s$, $X_{n-hep,f} = 0.035$.

It can be seen, that the computed and line-of-sight integrated results of the mass fraction of CH* correlate well with the photograph of the CH* taken through a narrow-band filter. To compare the CH* from the narrow-band filtered photograph and the CH* obtained computationally for more than one case, the same comparison is presented for initial temperature of $700\ K$. The corresponding photograph and the numerical results are shown in Figs. 7 and 8, respectively. Compared to $T_0 = 600\ K$, it can be seen that the diffusion flame region enlarges with the increasing temperature. Whereas, the width of the flame remains unchanged. The values extracted along the

dashed lines in the Figs. 7 and 8 show similar correlation as shown before for the initial temperature of 600 K in Fig. 6(c).

Conclusion

This study shows that the present chemical kinetic mechanism of 97 species is validated with excellent agreement with the experimental results. On top of that, and more importantly, the parametric study shows that the complex 2-D axisymmetric simulation methods are also in good agreement with the experiments. The lift-off height computed is less than 5% different from the experiments. Which, considering the complexity not only of the 2-D simulation methods but also of the high hydrocarbon fuel used in the simulations, is noteworthy.

Comparing the photographs of the CH* and the CH* obtained computationally, also proves that the simulations are copying the actual reality with relatively high precision. The computations, as well as the actual photographs from the experiments, both show the same tendency that with increasing temperature the diffusion region of the flame becomes larger while the width of the flame is unchanged. Thus, this study indicates that the present 97 species mechanism predicts the peak CH* concentration with high accuracy.

Quantitative correlation between the chemiluminescence peak-intensity and the heat release rate is provided. Therefore, the chemiluminescence can be used as the heat release marker for the tribrachial *n*-heptane laminar flames. This is an inexpensive alternative to laser techniques that can provide an information with effective spatial-resolution for combustion sensing.

This study is a part of the ongoing effort to study the tribrachial flames in low temperature regimes. However, first the chemiluminescent diagnostic is observed for the high temperatures as presented here.

Acknowledgement

This work was supported by Saudi Aramco.

References

[1] S. H. Chung, Proc. Combust. Inst. 31 (2007) 877–892.

[2] S. H. Chung, B. J. Lee, Combust. Flame 86 (1991) 62–72.

[3] B. J. Lee, S. H. Chung, Combust. Flame 109 (1997) 163–172.

[4] Y. S. Ko, T. M. Chung, S. H. Chung, KSME Int. J. 16 (2002) 1710–1718.

[5] J. Prager, H. N. Najm, M. Valorani, D. A. Goussis, Combust. Flame 158 (2011) 2128–2144.

[6] S. K. Choi, S. H. Chung, Combust. Flame In Press (2013).

[7] T. Kathrotia, U. Riedel, A. Seipel, K. Moshammer, A. Brockhinke, J. Appl. Phys. B 107 (2012) 571–584.

[8] S. M. Sarathy, S. Vranckx, K. Yasunaga, M. Mehl, P. Osswald, W. K. Metcalfe, C. K. Westbrook, W. J. Pitz, K. K.-Hoinghaus, R. X. Fernandes, H. J. Curran, Combust. Flame 159 (2012) 2028–2055.

[9] T. Lu, C. K. Law, Proc. Combust. Inst. 30 (2005) 1333–1341.

[10] A. G. Tomboulides, J. C. Y. Lee, S. A. Orszag, J. Sci. Comput. 12 (1997) 139–167.

[11] R. B. Bird, W. E. Stewart, E. N. Lightfoot, Transport phenomena, John Wiley & Sons, New York, 2007.

[12] T. Poinsot, Theoretical and Numerical Combustion, R.T. Edwards, Inc., 2005.

[13] T. P. Cofee, J. M. Heimerl, Combust. Flame 43 (1981) 273–289.

[14] O. Desjardins, B. Blanquart, G. Balarac, H. Pitsch, J. Comput. Phys. 227 (2008) 7125–7159.

[15] J. Kim, P. Moin, J. Comput. Phys. 59 (1985) 308–323.

[16] R. Falgout, J. Jones, U. Yang, in: A. Bruaset, A. Tveito (Eds.), Numerical Solution of Partial Differential Equations on Parallel Computers, Springer-Verlag, 2006, pp. 267–294.

[17] R. Barrett, M. Berry, T. F. Chan, J. Demmel, J. M. Donato, J. Dongarra, V. Eijkhout, R. Pozo, C. Romine, H. V. D. Vorst, Templates for the solution of linear systems: Building blocks for iterative methods, 1994.

[18] S. F. Ashby, R. D. Falgout, Nucl. Sci. Eng. 124 (1996) 145–159.

[19] C. Ji, E. Dames, Y. L. Wang, H. Wang, F. N. Egolfopoulos, Combust. Flame 157 (2010) 277–287.

[20] S. G. Davis, C. Law, Symp. Int. Combust. Proc. 27 (1998) 521–527.

[21] R. Seiser, H. Pitsch, K. Seshadri, W. J. Pitz, H. J. Curran, Proc. Combust. Inst. 28 (2000) 2029–2037.

[22] R. J. Kee, F. M. Rupley, J. A. Miller, Sandia Report SAND89-8009B, Technical Report, Sandia National Labs, Livermore, CA, 1993.

[23] R. J. Kee, J. F. Grcar, M. D. Smooke, J. A. Miller, Sandia Report SAND85-8240, Technical Report, Sandia National Labs, Livermore, CA, 1993.

[24] Y. L. Wang, A. T. Holley, C. Ji, F. N. Egolfopoulos, T. T. Tsotsis, H. J. Curran, Proc. Combust. Inst. 32 (2009) 1035–1042.

[25] R. Seiser, L. Truett, D. Trees, K. Seshadri, Symp. Int. Combust. Proc. 27 (1998) 649–657.

[26] J. Kojima, Y. Ikeda, T. Nakajima, Combust. Flame 140 (2005) 34–45.

[27] A. M. Cormack, Computed tomography: Proceedings of Symposia in Applied Mathematics 27 (1983) 35–42.

[28] C. J. Dasch, Applied Optics 31 (1992) 1146–1152.